The Astrophysical Journal Letters, 827:L41 (5pp), 2016 August 20 doi:10.3847/2041-8205/827/2/L41

LONG-TERM TREND OF SOLAR CORONAL HOLE DISTRIBUTION FROM 1975 TO 2014

K. Fujiki[1], M. Tokumaru[1], K. Hayashi[1], D. Satonaka[1], and K. Hakamada[2]
[1] Institute for Space-Earth Environmental Research (ISEE), Nagoya University, Furo-cho, Chikusa, Nagoya Aichi 464-8601, Japan; fujiki@isee.nagoya-u.ac.jp
[2] Department of Natural Science and Mathematics, Chubu University, 1200 Matsumoto-cho, Kasugai, Aichi 487-8501, Japan
Received 2016 June 8; revised 2016 August 5; accepted 2016 August 6; published 2016 August 19

ABSTRACT

We developed an automated prediction technique for coronal holes using potential magnetic field extrapolation in the solar corona to construct a database of coronal holes appearing from 1975 February to 2015 July (Carrington rotations from 1625 to 2165). Coronal holes are labeled with the location, size, and average magnetic field of each coronal hole on the photosphere and source surface. As a result, we identified 3335 coronal holes and found that the long-term distribution of coronal holes shows a similar pattern known as the magnetic butterfly diagram, and polar/low-latitude coronal holes tend to decrease/increase in the last solar minimum relative to the previous two minima.

Key words: Sun: activity – Sun: general – Sun: magnetic fields

1. INTRODUCTION

Coronal holes are extremely low density unipolar open magnetic field regions in the solar corona (Altschuler et al. 1972) and are usually identified by darker areas in X-ray (Timothy et al. 1975) and EUV (Munro & Withbroe 1972) observations, and as brighter areas by chromospheric He I 1083 nm (e.g., Henney & Harvey 2005) observation. While there is difficulty in identifying the coronal-hole area using image-based analysis, many trials have been made so far not only for the interests of solar science but also to meet the need for solar-wind predictions for space-weather application (Henney & Harvey 2005; Scholl & Habbal 2008; Tlatov et al. 2014; Reiss et al. 2015).

Another approach for the identification of coronal holes is by deriving the photospheric footpoints of the open magnetic flux using an appropriate model for coronal magnetic field calculation and observation of the photospheric magnetic field. Neugebauer et al. (1998) compared several coronal magnetic field models such as MHD and different potential-field calculations, and concluded that photospheric footpoints of open field lines calculated from the models generally agree with He I 1083 nm observations.

Owens et al. (2014) introduced photospheric distances between footpoints obtained from potential-field calculations and projected them onto the source surface for automated detection of pseudostreamers (Wang et al. 2007). The pseudostreamer always differentiates the boundary of two or more magnetic fluxes from isolated clusters of open field footpoints. Therefore, this method can be used for automated prediction of coronal holes.

In this study we develop a coronal hole automated prediction technique and construct a coronal-hole database from 1975 to 2014 (Carrington rotations (CR) from 1625 to 2165).

2. DATA AND ANALYSIS

In order to identify coronal holes in each CR, we used a potential-field-source-surface (PFSS) model (Altschuler & Newkirk 1969; Schatten et al. 1969) to extrapolate the magnetic field from the photosphere to the source surface. The PFSS calculation code in this study was developed by Hakamada (1995), and the coronal magnetic field was calculated using spherical harmonic coefficients up to the 90th order. Synoptic Magnetogram data from CR 1625 to CR 2165, with a spatial resolution of 1° in longitude obtained at the National Solar Observatory/Kitt-Peak (NSO/KP), were used as an input for the PFSS calculation. We excluded CRs in which the magnetogram did not cover all data points except for a polar region gap caused by the inclination of the solar rotation axis. The excluded CRs in this analysis are 1625, 1631, 1632, 1635, 1637, 1639, 1640–1648, 1650, 1658, 1661, 1663, 1665, 1837, 1854, 1860, 1973, 1981, 2014–2016, 2019, 2026, 2033, 2035, 2040, 2041, 2059, 2063, 2090–2099, 2119, 2127, 2152–2155, 2157, and 2163.

We first remapped the magnetic field distribution on the source surface of 2.5 solar radii ($R_\odot$) onto regularly gridded points 1° × 1° in latitude and longitude, and then determine the photospheric magnetic field and position by tracing each magnetic field line from each grid point on the source surface. We used a similar algorithm adopted by Owens et al. (2014) for the identification of pseudostreamers. We define a relative angular distance, $\alpha = \delta\alpha_p/\delta\alpha_s$, with heliocentric-angle separation between adjacent pixels on source surface $\delta\alpha_s$ and between magnetically connected footpoints on photosphere $\delta\alpha_p$ (Figure 1(a)). In this study, we define a coronal hole as a cluster of magnetic footpoints with the α smaller than 10. Each open field low-α cluster region split by large-α lanes is recognized by applying an image-based region-growing algorithm (e.g., Petrou & Bosdogianni 2004). Figure 1(c) elaborates the positions of the predicted coronal holes on the photosphere, with red (blue) plots indicating the boundary of positive-(negative-)polarity open field regions. We calculated the areas on the source surface (A_s) and photosphere (A_p), averages of the magnetic field on the source surface (B_s) and photosphere (B_p), and flux expansion factor (f) as

$$A_s = \sum_i A\cos\theta_i, \quad A_p = \frac{\sum_i A\cos\theta_i B_{s,i}}{B_{p,i}},$$
$$f = \frac{A_s}{A_p}\left(\frac{R_s}{R_\odot}\right)^2, \quad B_s = \frac{\sum_i B_{s,i}\cos\theta_{s,i}}{\sum_i \cos\theta_{s,i}},$$
$$B_p = \left(\frac{R_s}{R_\odot}\right)^2 f B_s,$$

where A and θ_i are the physical area of each data grid point at the equator on the source surface and the latitude of the ith

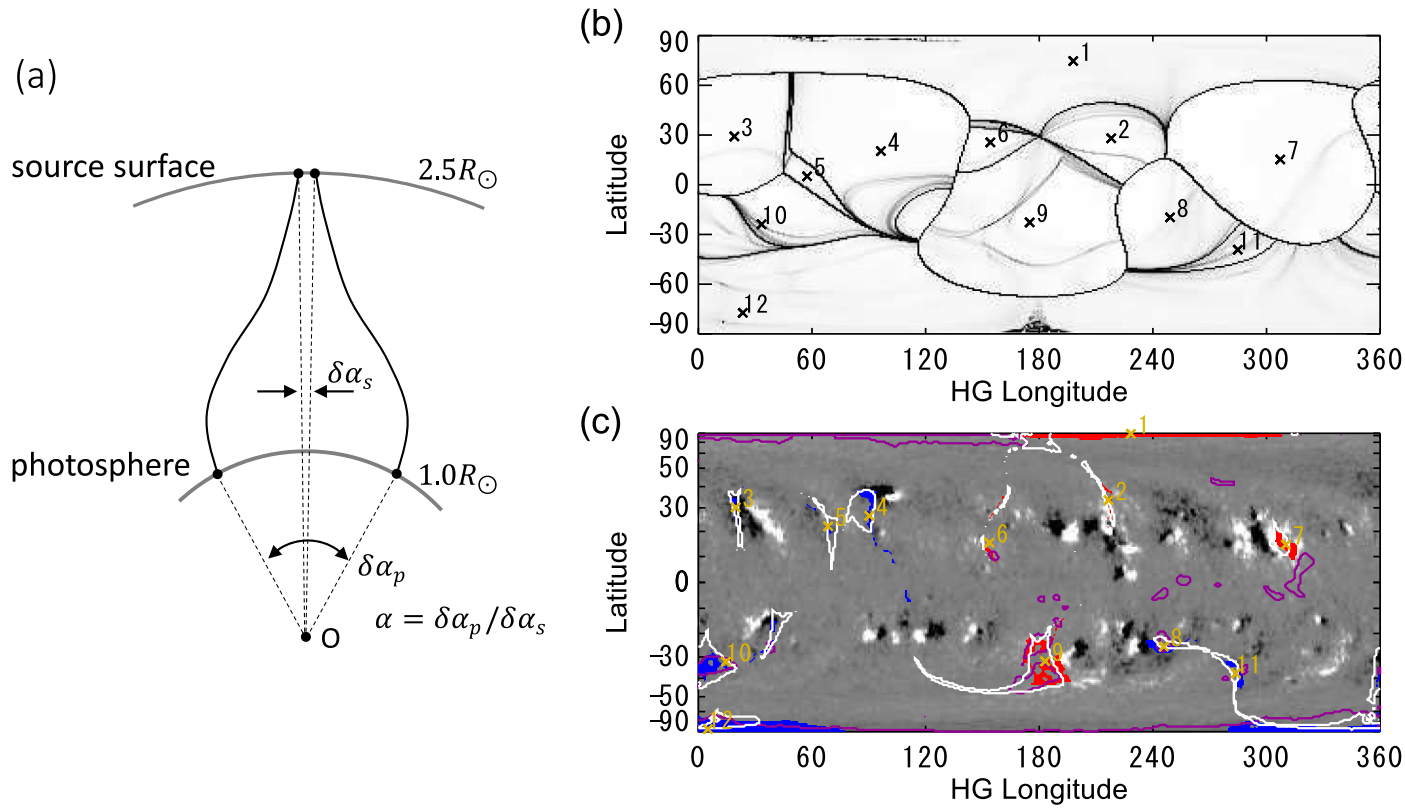

Figure 1. (a) Definition of α. Black curves represent magnetic field lines originating in different coronal holes and encountering at adjacent locations on the source surface. (b) Example of the distribution of α for CR1949. The α is mapped on the source surface with a saturation level of 10. The "x" mark represents the position of the COG of each segment distinguished by $\alpha = 10$. (c) Coronal holes predicted by the PFSS analysis with positive (red) and negative (blue) polarities. The "x" mark represents the position of the COG of each predicted coronal hole. The number at each COG position represents the serial number of the coronal hole. The white contour shows a result of the PFSS calculation using a synoptic magnetogram at WSO. The purple contour shows a result of an automated detection using He I 1083 nm observation at KP/NSO.

pixel on the source surface. $B_{s,i}$ and $B_{p,i}$ are the magnetic field of the$i$th pixel on the source surface and its photospheric counterpart, and $R_s = 2.5R_\odot$ is the radius of the source surface. Detected coronal holes are numbered in descending order of photospheric latitudes of the center-of-gravity (COG) in each CR. The COG is calculated by averaging positions of footpoints in each cluster with a weight of $A \cos\theta_i B_{s,i}/B_{p,i}$.

We identified 3574 coronal holes with the automated prediction algorithm. Then we filtered out coronal holes with a small area and magnetic field strength. The thresholds are determined by the pixel size of the synoptic magnetogram at the solar equator, $\sim 1.5 \times 10^8$ km^2, and maximum magnetic field fluctuation level 3.5 G (1σ) derived by Gaussian-fitting the histogram of the magnetic field, respectively. Consequently, we obtained a database of 3335 coronal holes.

3. RESULTS AND DISCUSSION

The purple contour in Figure 1(c) shows boundaries of coronal holes derived through an automated algorithm from the He 1083 nm observation. The boundary is determined by using a threshold of the upper-side half-maximum of the intensity distribution. Coronal holes labeled 2, 3, 4, and 5 are missing in the He 1083 nm observation. Coronal holes 2, 3, and 4 were nearby active regions and are candidates for the origins of the slow solar wind (Kojima et al. 1999; Sakao et al. 2007). On the other hand, coronal holes identified by the He 1083 nm threshold at 240°–300° longitude and around zero degrees latitude are not predicted by the automatic algorithm. In this examined period (CR1949), 7 out of 12 coronal holes are overlapped by coronal holes detected in the He 1083 nm observation.

In order to check how much the PFSS solutions using different observatory data differ, we conduct identical calculations using Wilcox Solar Observatory (WSO) data and compare the PFSS solutions. The WSO has been carrying out solar magnetic observation since 1976 and providing consistent data, which were often used as a calibrator for new instruments. The footpoint clusters obtained from WSO (white) data coincide well with those from NSO/KP data. The near-equator He I coronal holes that the KP/NSO data could not predict were not predicted with the WSO data either. From these, the discrepancy between the coronal hole detected by PFSS and He I 1083 nm is not caused by the uncertainty of input data in the PFSS calculation. The synoptic He I1083 nm map is made from strip images around the central meridian of the full disk observation. In this sense, coronal-hole distribution observed with He I 1083 nm is purely a stack of snapshots. On the other hand, open flux distribution is determined by the global distribution of the magnetic field on the Sun. Therefore, consistency is not that important for smaller coronal holes because some might be short-lived or transient coronal holes.

Figure 2(a) is the probability distribution of coronal-hole areas derived from the PFSS analysis (gray) and He I 1083 nm synoptic map (white) normalized to the solar surface, $A_{\rm Sun} = 6.1 \times 10^{12}$ km^2. Coronal holes observed with He I

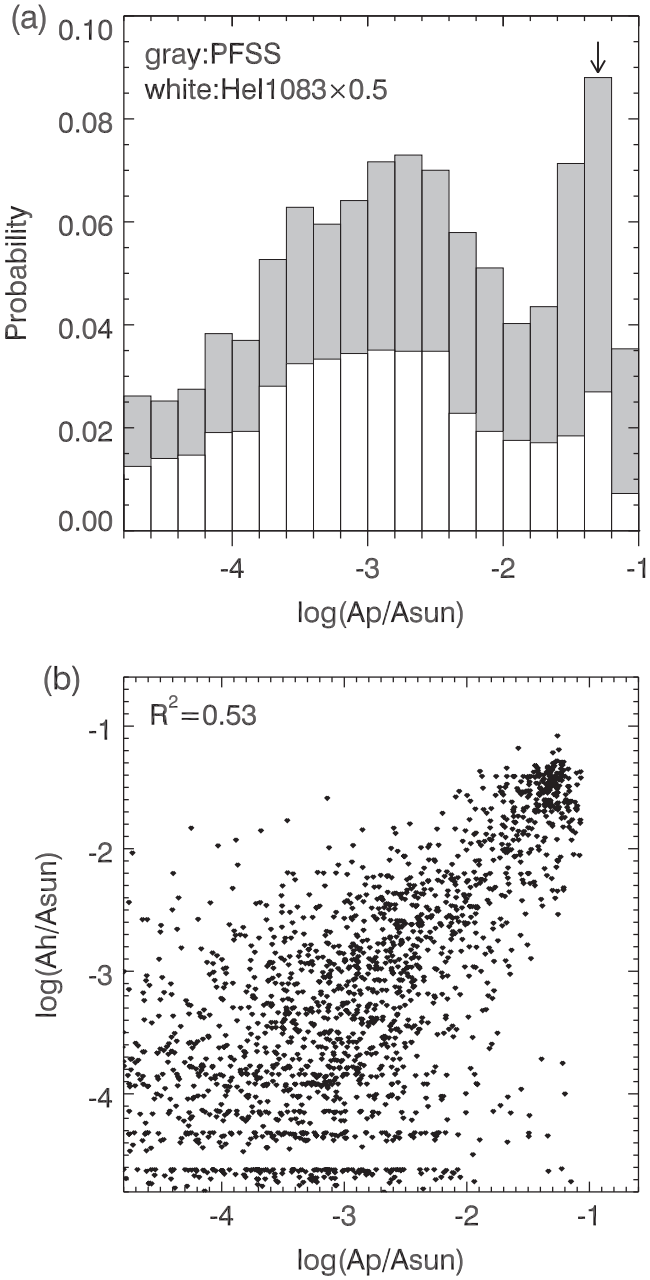

Figure 2. (a) Probability distribution of coronal-hole areas. Gray and white histograms are derived from PFSS calculation and He I 1083 nm observation, respectively, predicted from CR 2165 to CR 2020. Arrow shows a higher peak at $A_p/A_{\rm Sun} = 10^{-1.3}$. (b) Scatter plot of coronal-hole areas derived by PFSS calculation (A_p) and those from He I 1083 nm observations (A_h).

1083 nm are detected automatically with almost the same threshold (area $>1 \times 10^8$ km^2 and separation angle $\alpha_{\rm He\,I} > 10°$). Then, we use only the coronal hole nearest to the COG of each predicted coronal hole to make the probability distribution. Both histograms show similar distributions and two peaks at the same coronal-hole areas. The peak around $10^{-1.3}$, marked by an arrow, corresponds to a polar coronal hole. This result is consistent with that of Hess Webber et al. (2014) using synoptic data obtained with the Extreme ultraviolet Imaging Telescope and Michelson Doppler Imager on board the *SOlar and Heliospheric Observatory*. By contrast, the major distribution is found around $A_p/A_{\rm Sun} = 10^{-2.7}$ in both histogram and is 6 times larger than that detected using synoptic data obtained with observations of He I 1083 nm, $A_p/A_{\rm Sun} \sim 10^{-3.5}$ (Tlatov et al. 2014). One reason for the large difference is attributed to the detection algorithm. In our algorithm we use the separation angle to identify a coronal hole, which considers a group of small coronal holes as a single large one. Figure 2(b) is a correlation plot between areas of predicted and observed coronal holes. The correlation coefficient is 0.53 and a scatter from the correlation line decreases for larger coronal holes. Although a one-to-one correspondence between the predicted and detected coronal-hole areas include larger errors, especially for smaller coronal holes, the good linearity obtained supports the reliability of the predicted area for statistical analysis.

Figure 3 displays the long-term latitudinal distribution of the coronal-hole locations. The pattern of appearance of coronal holes is very similar to the butterfly diagram of magnetogram data. Although the butterfly pattern of open magnetic footpoint was also reported by Obridko & Shelting (1999), Wang et al. (2009), and Wang (2016), the distribution of coronal-hole COGs is more remarkable. At the beginning of each solar cycle, coronal holes with the same polarity as the polar field of the hemisphere appear at mid-latitude up to ~40°. The CH group diffuses toward the equator as the solar activity increases. Coronal holes with polarity opposite that of the polar field in the hemisphere appear with a time lag of almost one year, and move toward the pole along magnetic flux transport lanes. In particular, tracks of coronal holes toward the pole were clearly observed during the polarity reversal in the solar maximum. The pre-existing polar coronal holes shrank before the polarity reversal, and the COG latitude deviated from the pole. This is a natural consequence of the weakening of the dipole magnetic field component, which is dominant in the solar minimum. The behavior of the coronal-hole distribution in latitude and time indicates a strong connection between low-latitude hole formation and sunspot activity, and between polar hole evolution and the poleward transport of flux from the sunspot latitudes (see, e.g., the flux-transport simulations of Wang et al. 2002).

Figure 4(a) shows the temporal variation of ±9-rotation running-averaged coronal-hole areas appearing around the polar region ($|\theta| > 50°$) and middle to low-latitude regions ($|\theta| < 50°$). We can see that the total area of polar coronal holes peaks around solar minima and shrinks around solar maxima while that of mid-/low-latitudes coronal holes change in the opposite way in both periods. As for long-term variations, the total area of the polar coronal hole around solar minima gradually decreases by 34% over the three solar cycles. On the other hand, the total area of lower-latitude coronal holes increase five times for the same period. The increase in lower-latitude coronal holes can be explained by the weakening of the polar field. Wang et al. (2009) examined the dependence of coronal-hole areas at polar and low latitudes on polar field strength using a computational experiment. They concluded that the stronger polar field has the effects of enlarging the polar coronal hole and suppressing the low-latitude coronal hole, which is a consequence of the fact that the stronger pole-to-pole closed-field dipole structures suppress the escape of the middle latitude fluxes to interplanetary space.

The 22 year periodicity in galactic cosmic-ray (GCR) flux observed at the Earth has been studied extensively so far. The GCR flux exhibits alternating peak values at solar minimum phase: sharp ($qA < 0$) and flat-topped peaks ($qA > 0$)

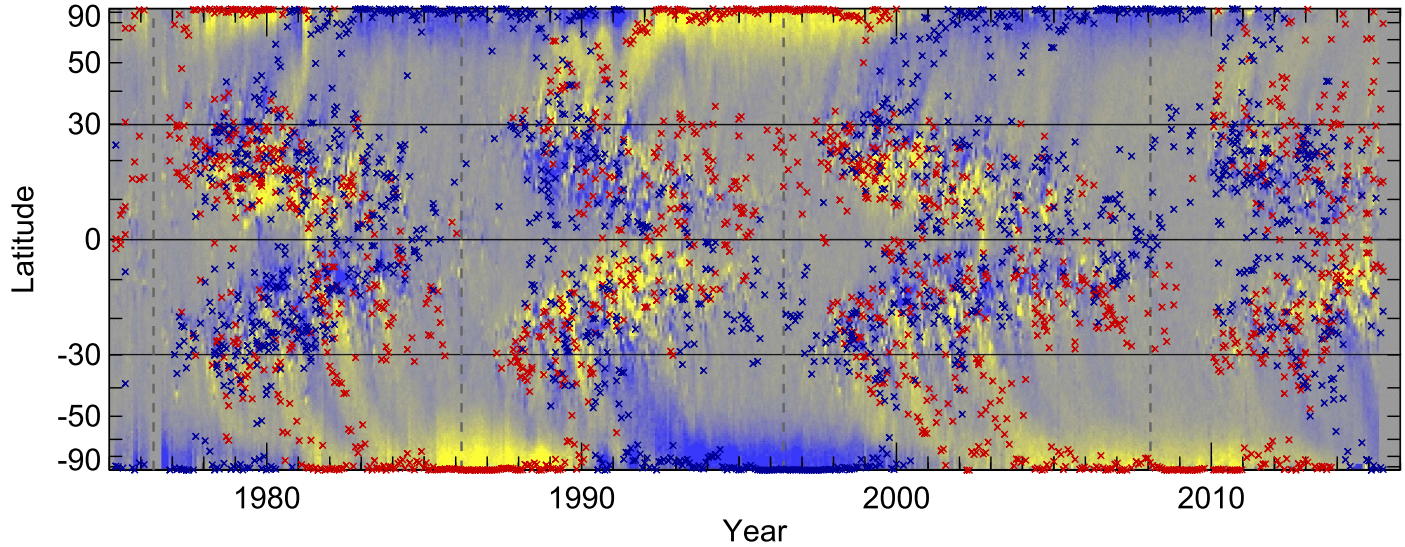

Figure 3. Latitude distribution of 2870 coronal holes. The "x" mark represents the COG latitude of each coronal hole. The background color image is the magnetic butterfly map (Hathaway 2010) scaled as −10 G (blue), 0 G (gray), and 10 G (yellow). The latest version is available at http://solarscience.msfc.nasa.gov/images/magbfly.jpg.

(e.g., Webber & Lockwood 1988). The parameters q and A denote the sign of the charge of the particle and the polarity of the north polar field of the Sun. The product qA represents the direction of drift motion of the charged particle in the solar polarity cycle. Thomas et al. (2014) demonstrated that heliospheric magnetic field (HMF) structures are different during the declining phase of the positive- and negative-qA cycles using space-age data. They suggested that the 22 year cycle in GCR flux is at least partly the result of direct modulation by the HMF. The polar coronal-hole areas in the 1990s ($qA > 0$) are very stable in comparison with the previous solar cycle and the following one with negative qA. The variation of the polar coronal-hole area in three polarity cycles shows patterns of variation similar to the neutron monitor, which is shown as a black curve in Figure 4(a). The cross-correlation function between the polar coronal-hole area and the neutron monitor takes a maximum value at a time lag of 13 CRs (∼1 year), which is equivalent to the propagation time of the solar wind from the Sun to the termination shock, as shown in Figure 4(b). The tilt angle of the HMF, determined by the ratio of the magnetic dipole to the multipole components of the Sun, is one of the key parameters of the GCR modulation as indicated in a comparative study between solar magnetic field, IMF, and GCR flux at 1 au (Cane et al. 1999). The area of the polar coronal hole is an observable indicator of the dipole component of the solar magnetic field, and it might be another useful parameter of GCR modulation.

Finally, from the viewpoint of solar wind research, we obtained a useful database on the coronal hole as the source of solar wind in this study. Empirical relationships between solar wind speed and coronal-hole parameter, such as the physical area of the coronal hole (Nolte et al. 1976) and flux tube expansion factor (Wang & Sheeley 1990; Arge & Pizzo 2000), have been investigated. We plan on using our database to improve the relationship between the solar wind speed and flux tube expansion factor (Wang & Sheeley 1990) in the future. Furthermore, the similarity of the sunspot and coronal-hole butterfly patterns gives insight into how the global structures of the solar wind and HMF in the period before solar magnetic field observations started in 1930s can be reconstructed, because we have sketches and photographs of solar sunspots from as early as the 17th century.

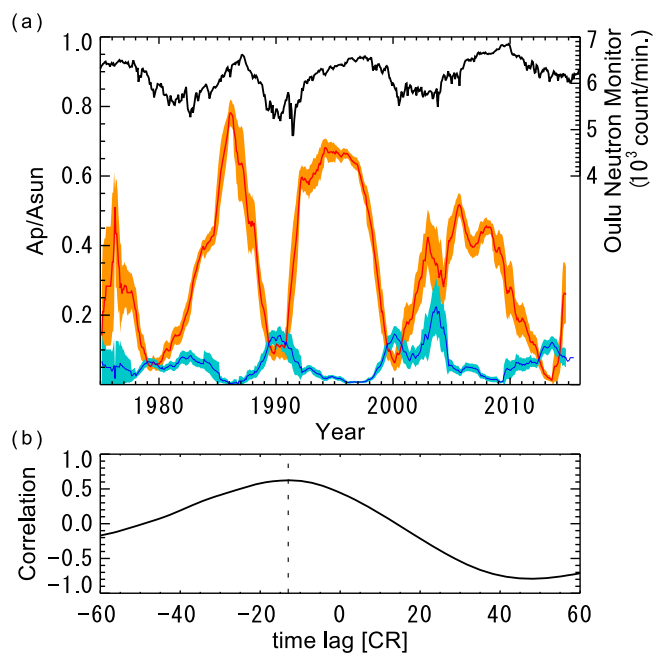

Figure 4. (a) Variations of coronal-hole areas. Red and blue curves represent variations in the integrated area of coronal holes appearing at high latitude ($|\theta| > 50°$) and low latitude ($|\theta| < 50°$), averaged over ±9 solar rotations. Orange and cyan belts denote error of $1.96\sigma/\sqrt{n}$ of the red and blue profiles, where n is the number of coronal holes. Black curve represents the 27 day averaged count of the neutron monitor at the Oulu Cosmic Ray Station. (b) Cross-correlation between the area of polar coronal hole and the count of neutron monitor as a function of the time lag of the Carrington rotation. Dashed line denotes the peak of the function.

We are grateful to the National Solar Observatory/Kipp Peak for the use of their synoptic magnetogram and synoptic He I 1083 nm data. We are also thankful to the Wilcox Solar Observatory for the use of synoptic magnetogram data. We

acknowledge the use of the global photospheric magnetic field pattern from 1980 to 2015 (http://solarscience.msfc.nasa.gov/images/magbfly.jpg) operated by the Solar Physics Group at NASA's Marshall Space Flight Center. We would like to thank the Oulu Cosmic Ray Station for the use of the neutron monitor data (http://cosmicrays.oulu.fi/). This work was supported by the JSPS Grant-in-Aid for Scientific Research A (25257079).

REFERENCES

Altschuler, M. D., & Newkirk, G. 1969, SoPh, 9, 131
Altschuler, M. D., Trotter, D. E., & Orrall, F. Q. 1972, SoPh, 26, 354
Arge, C. N., & Pizzo, V. J. 2000, JGR, 105, 10465
Cane, H. V., Wibberenz, G., Richardson, I. G., & von Rosenvinge, T. T. 1999, GeoRL, 26, 565
Hakamada, K. 1995, SoPh, 159, 89
Hathaway, D. H. 2010, LRSP, 7, 1
Henney, C. J., & Harvey, J. W. 2005, in ASP Conf. Ser. 346, Large-scale Structures and their Role in Solar Activity, ed. K. Sankarasubramanian, M. Penn, & A. Pevtsov (San Francisco, CA: ASP), 261
Hess Webber, S. A., Karna, N., Pesnell, W. D., & Kirk, M. S. 2014, SoPh, 289, 4047
Kojima, M., Fujiki, K., Ohmi, T., et al. 1999, JGR, 104, 16993
Munro, R. H., & Withbroe, G. L. 1972, ApJ, 176, 511
Neugebauer, M., Forsyth, R. J., Galvin, A. B., et al. 1998, JGR, 103, 14587
Nolte, J. T., Krieger, A. S., Timothy, A. F., et al. 1976, SoPh, 46, 303
Obridko, V. N., & Shelting, B. D. 1999, SoPh, 187, 185
Owens, M. J., Crooker, N. U., & Lockwood, M. 2014, JGRA, 119, 36
Petrou, M., & Bosdogianni, P. 2004, Image Processing the Fundamentals (Chichester: Wiley)
Reiss, M. A., Hofmeister, S. J., De Visscher, R., et al. 2015, JSWSC, 5, A23
Sakao, T., Kano, R., Narukage, N., et al. 2007, Sci, 318, 1585
Schatten, K. H., Wilcox, J. M., & Ness, N. F. 1969, SoPh, 6, 442
Scholl, I. F., & Habbal, S. R. 2008, SoPh, 248, 425
Thomas, S. R., Owens, M. J., & Lockwood, M. 2014, SoPh, 289, 407
Timothy, A. F., Krieger, A. S., & Vaiana, G. S. 1975, SoPh, 42, 135
Tlatov, A., Tavastsherna, K., & Vasil'eva, V. 2014, SoPh, 289, 1349
Wang, Y.-M. 2016, SSRv, in press
Wang, Y.-M., Robbrecht, E., & Sheeley, N. R., Jr. 2009, ApJ, 707, 1372
Wang, Y.-M., & Sheeley, N. R., Jr. 1990, ApJ, 355, 726
Wang, Y.-M., Sheeley, N. R., Jr., & Lean, J. 2002, ApJ, 580, 1188
Wang, Y.-M., Sheeley, N. R., Jr., & Rich, N. B. 2007, ApJ, 658, 1340
Webber, W. R., & Lockwood, J. A. 1988, JGR, 93, 8735